ACS OMEGA

Article

Cite This: ACS Omega 2019, 4, 11112−11118

http://pubs.acs.org/journal/acsodf

Giant Chemical and Excellent Synergistic Raman Enhancement from a 3D $MoS_{2-x}O_x$−Gold Nanoparticle Hybrid

Avijit Pramanik, Ye Gao, Kaelin Gates, Salma Begum, and Paresh Chandra Ray*

Department of Chemistry and Biochemistry, Jackson State University, Jackson 39217, Mississippi, United States

Supporting Information

ABSTRACT: Raman spectroscopy fingerprinting features many technological applications. For this purpose, the weak Raman signals need to be boosted dramatically by surface-enhanced Raman spectroscopy (SERS), which provides immense Raman enhancement via plasmonic and chemical mechanisms (CM). In this manuscript, we reveal the giant chemical as well as extremely high SERS enhancement from a three-dimensional $MoS_{2-x}O_x$−gold nanoparticle (GNP) hybrid, which has capability for ultrasensitive label-free sensing of chemical and biological molecules. Notably, reported data show that the chemical enhancement for the $MoS_{2-x}O_x$ surface is ∼10^5, which is comparable with the plasmonic enhancement factor (EF) by GNP. Reported data show that the total Raman EF is ∼10^{13} from the GNP−$MoS_{2-x}O_x$ hybrid. Intriguingly, combined experimental and theoretical finite difference time domain stimulation modeling findings show that the synergistic effect of electromagnetic mechanism and CM is responsible for huge SERS enhancement. Experimental results demonstrate that a proposed hybrid SERS platform can be used for fingerprint sensing of different multiple drug resistance bacteria at 5 cfu/mL concentration. Importantly, the current manuscript provides a good strategy for manipulating the SERS sensitivity to 13 orders of magnitude, which is instrumental for next-generation technological applications of Raman spectroscopy.

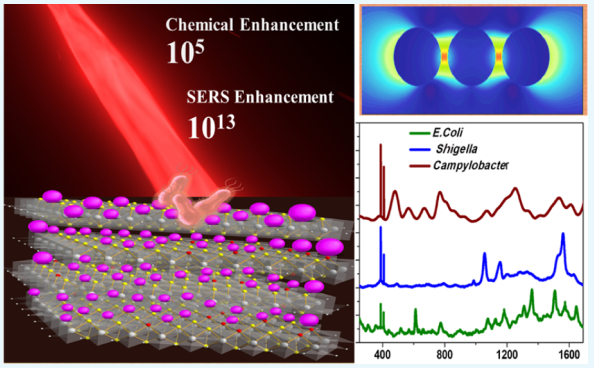

1. INTRODUCTION

Raman spectroscopy is highly promising for fingerprint identification of chemical and biological molecules.[1,2] Because of the above unique ability and multiplex detection capability, the Raman technique is highly valuable in forensics, homeland security, and medical diagnosis industry.[3,4] However, because of the inherently low cross section of Raman scattering, it has not been used as an analytical tool for practical applications.[5,6] In last few decades, it has been reported that extremely weak Raman signals can be dramatically enhanced by surface-enhanced Raman scattering (SERS) via plasmonic and chemical boosting mechanisms.[7,8] In SERS, plasmonic enhancement occurs in the presence of plasmonic nanoparticles via electromagnetic mechanism (EM).[9,10] On the other hand, chemical enhancement occurs via chemical mechanism (CM), which originated from the charge transfer between the Raman active molecule and the SERS substrate.[11,12] In the last 2 decades, we and other groups have reported different types of SERS materials which are based on the noble plasmonic metal nanoparticle, where Raman intensity can be enhanced several orders of magnitude (10^6 or higher) via EM.[13,14] On the other hand, for most of the reported SERS substrate, the reported chemical enhancement factor (EF) is ∼10^2.[15,16] Recently, the SERS substrate based on two-dimensional (2D) transition-metal dichalcogenides has been reported,[17−25] where the chemical EF can be much higher than 10^2, and in this case, the laser excitation can be resonant to charge transfer and exciton transitions in an analyte 2D system.[26−32] For real-life applications, an SERS probe should possess strong electromagnetic as well as strong chemical enhancement capability for providing excellent sensitivity. Herein, we report huge chemical (CM) and electromagnetic (EM) enhancements from a three-dimensional (3D) $MoS_{2-x}O_x$−gold nanoparticle (GNP) hybrid. Experimental data reported here indicate that the chemical EF is ∼10^5 from the $MoS_{2-x}O_x$ surface, which is comparable with the plasmonic enhancement by GNP. Reported data demonstrated that oxygen incorporation on MoS_2 can effectively improve the SERS performance via a strong chemical enhancement mechanism. On the other hand, the total SERS enhancement from the GNP−$MoS_{2-x}O_x$ hybrid was observed to be ∼10^{13}. Our experimental and theoretical finite difference time domain (FDTD) stimulation modeling[22,23] shows that the synergistic effect of EM and CM is responsible for huge SERS enhancement. To demonstrate that $MoS_{2-x}O_x$−GNP-based ultrasensitive SERS is versatile for fingerprinting biological analysis, we have shown that an SERS platform can be used for fingerprint sensing of different

Received: March 28, 2019
Accepted: May 24, 2019
Published: June 25, 2019

DOI: 10.1021/acsomega.9b00866
ACS Omega 2019, 4, 11112−11118

multiple drug resistance bacteria such as carbapenem-resistant *Escherichia coli*, drug-resistant *Shigella*, and *Campylobacter*, at 5 cfu/mL concentration.

2. RESULTS AND DISCUSSION

As shown in Figure 1, we used a three-step method for the synthesis of a 3D $MoS_{2-x}O_x$−GNP hybrid. In the first step, a

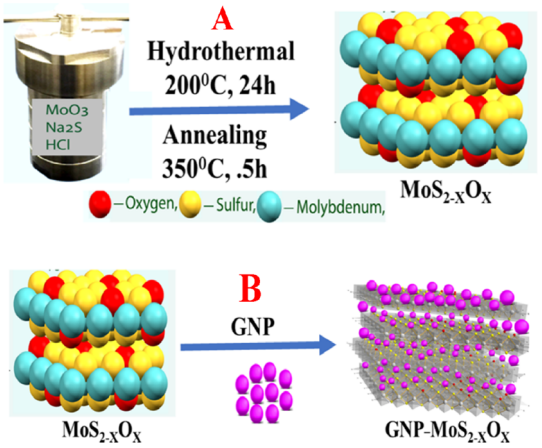

Figure 1. (A) Scheme shows the synthetic route we have used to develop 2D $MoS_{2-x}O_x$ via a hydrothermal process as well as an annealing process. (B) Scheme shows the synthetic route we have used to develop GNP−$MoS_{2-x}O_x$ nanocomposites.

facile hydrothermal synthetic method was used for the synthesis of MoS_2 nanosheets. Experimental details have been reported in the Experimental Section. In brief, in the first step, molybdenum(VI) oxide powder, sodium sulfide (Na_2S), and HCl were mixed and kept into a Teflon-lined stainless steel autoclave. After that, the mixture was heated for 200 °C overnight. A black precipitate was obtained by centrifugation from the final reaction products and then the 2D MoS_2 was washed with distilled water and ethanol. Because it is now well-known that oxygen incorporation is the effective way to improve the SERS performance of nonmetal oxide semiconductors,[20−22] in the next step, we have synthesized a 2D $MoS_{2-x}O_x$ nanosheet. For this purpose, we have developed a $MoS_{2-x}O_x$ nanosheet, via annealing of 2D MoS_2 at 350 °C temperature in air. In the third step, we have developed a 3D $MoS_{2-x}O_x$−GNP hybrid. For this purpose, we have used GNP as a linker between 2D $MoS_{2-x}O_x$ nanosheets to form the 3D $MoS_{2-x}O_x$−GNP hybrid, via a −Mo−S−Au− bond.

After that, we have used different electron microscopic and spectroscopic techniques[6,11−16] to characterize the 3D $MoS_{2-x}O_x$−GNP hybrid as reported in Figures 2A−C and S1A−G. The elemental molar ratios of the 3D $MoS_{2-x}O_x$−GNP hybrid were determined using energy-dispersive X-ray (EDX), X-ray diffraction (XRD), and Raman data. Figure S1A reports the transmission electron microscopy (TEM) image which indicates that the size of the GNP we have synthesized is about 25 nm. Figure S1B reports the scanning electron microscopy (SEM) which shows the morphology of 2D $MoS_{2-x}O_x$ nanosheets. Figure 2A reports the SEM image which shows the morphology of the 3D $MoS_{2-x}O_x$−GNP hybrid, which indicates that a porous structure is developed with a pore diameter varying from 10 to 400 nm. Both Figures 2A and S1C show the formation of a "hot spot" by the GNP on the $MoS_{2-x}O_x$ nanosheets. Figure S1E shows the EDX data

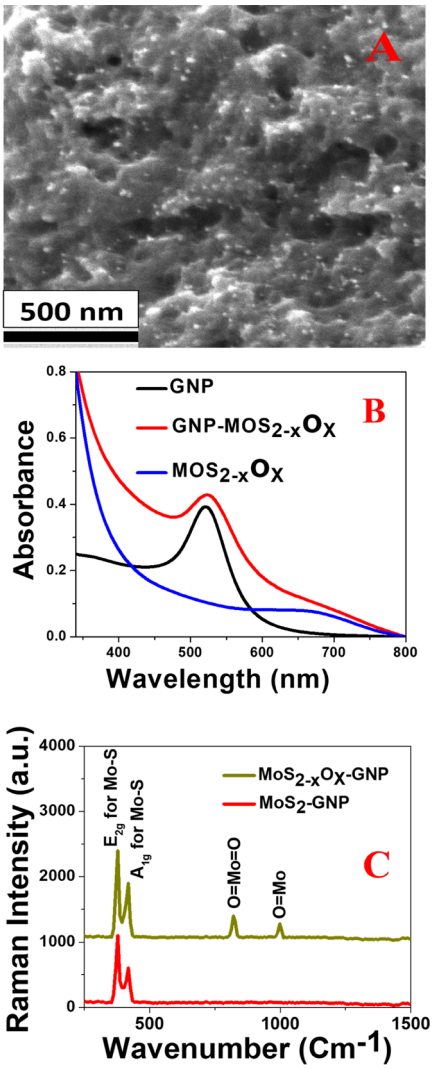

Figure 2. (A) SEM image shows the morphology of $MoS_{2-x}O_x$−GNP hybrid. (B) Extinction spectra from $MoS_{2-x}O_x$−GNP hybrid, GNP, and $MoS_{2-x}O_x$. (C) Raman spectra from $MoS_{2-x}O_x$−GNP hybrid and MoS_2−GNP hybrid.

from the $MoS_{2-x}O_x$−GNP hybrid, which clearly shows the presence of Mo, S, O, and Au. Similarly, Figure S1F shows the EDX data from MoS_2, before annealing, which clearly shows the presence of Mo and S.

Figure S1G shows the powder XRD data from the $MoS_{2-x}O_x$−GNP hybrid, which shows the presence of (002), (100), (104), and (201) reflection for MoS_2,[20−23] (020) reflection for MoO_3,[16−19] and (111) and (3111) reflection for GNP. Figure 2B shows the absorption spectra for GNP, 2D $MoS_{2-x}O_x$ nanosheets, and 3D $MoS_{2-x}O_x$−GNP hybrid. Reported data clearly indicate a broad plasmon band from the 3D $MoS_{2-x}O_x$−GNP hybrid which is due to the aggregation of GNP on the 3D hybrid, as shown in the TEM and SEM images reported in Figures S1C and 2A. To compare the Raman spectra between the $MoS_{2-x}O_x$−GNP hybrid and the MoS_2−GNP hybrid, we have also synthesized the MoS_2−GNP hybrid. For this purpose, we have used a GNP as a linker between 2D MoS_2 nanosheets to form the MoS_2−GNP hybrid, via a −Mo−S−Au− bond. Experimental details have been reported in the Supporting Information. The TEM image from the MoS_2−GNP hybrid, as reported in Figure

DOI: 10.1021/acsomega.9b00866
ACS Omega 2019, 4, 11112−11118

S1D, clearly shows the aggregation of GNP on the MoS_2 surface. Figure 2C shows that the Raman spectra from the 3D $MoS_{2-x}O_x$−GNP hybrid and MoS_2−GNP hybrid clearly indicate the presence of an in-plane (E_{2g}) Raman band at ∼384 cm^{-1} and an out-of-plane (A_{1g}) Raman band at ∼409 cm^{-1}, which is due to Mo−S vibration of MoS_2.[20−23] We have observed a (E_{2g}) Raman band and a (A_{1g}) Raman band for $MoS_{2-x}O_x$−GNP hybrid, as well as for MoS_2−GNP hybrid. Similarly, as reported in Figure 2C, we have also observed Raman peaks at ∼820 and ∼996 cm^{-1}, which are due to the Mo═O vibration.[19−22] Raman peaks at ∼820 and ∼996 cm^{-1} are only observed for the $MoS_{2-x}O_x$−GNP hybrid, which has been developed after annealing of MoS_2, as we have discussed previously.

Because Raman EF is most important for a Raman substrate, we have measured Raman EF using a 4-aminothiophenol (4-ATP) and Rh-6G dye. For the Raman EF measurement, we have used a portable Raman probe, where a continuous wavelength 670 nm diode-pumped solid-state laser was used as the excitation source. We have used fiber optics probe for excitation and data collection.[6,11−16] Experimental details are reported in the Experimental Section. Figure 3A shows strong Raman spectra from 4-ATP (10^{-6} M) on $MoS_{2-x}O_x$ surface. On the other hand, in the same condition, we have not observed any Raman peak from 4-ATP (10^{-6} M), when a bulk sample was used. Reported Raman data reported in Figure 3A show that dominated vibrational peaks are due to the a_1 vibrational mode peaks and these are ν(CC + NH_2 bend) at ∼1590 cm^{-1} and ν(CS) at ∼1078 cm^{-1}.[5−8] As reported in Figure 3A, we have also observed Raman peaks due to b_2 modes, at ∼1435 cm^{-1} due to the CC str in Ph ring + NH_2 rock, and at ∼1170 cm^{-1} due to CH bend vibration.[10−13]

As reported in Figure 3A, we have observed a clear 1078 cm^{-1} vibrational band from ATP in the bulk and on all surfaces, and as a result, we have used 1078 cm^{-1} vibrational band intensity for Raman EF calculation. From the Raman spectra, we have measured the Raman EF using the following equation.[10−12]

$$G = [I_{MoS_{2-x}O_x}]/[I_{bulk}] \times [M_{bulk}]/[M_{ads}] \quad (1)$$

where $I_{MoS_{2-x}O_x}$ is the intensity of 1078 cm^{-1} vibrational mode from 4-ATP on $MoS_{2-x}O_x$ surface. Similarly, I_{bulk} is the intensity of 1078 cm^{-1} vibrational band in the absence of $MoS_{2-x}O_x$ surface. M_{bulk} is the number of 4-ATP used in the bulk experiment without $MoS_{2-x}O_x$ surface and M_{ads} is the number of 4-ATP used for the Raman experiment on $MoS_{2-x}O_x$ surface. For bulk experiment, a Si/SiO_2 wafer was used as the normal Raman reference. For Raman experiment on all different surfaces, we have assumed that the analytes were distributed uniformly on the surface. The number of molecules is calculated using a laser spot size of 40 μm. From the experimental data on $MoS_{2-x}O_x$ surface as reported in Figure 3A, we found out that the EF is ∼1.3×10^5. Because of the lack of surface plasmons in the visible light for $MoS_{2-x}O_x$ surface, the observed huge Raman enhancement on $MoS_{2-x}O_x$ surface can be attributed to the chemical enhancement mechanism.

The huge chemical enhancement on $MoS_{2-x}O_x$ surface is due to the photon-induced charge transfer from the $MoS_{2-x}O_x$ surface to the adsorbed 4-ATP molecule. As reported in Figure S2C in the Supporting Information, the GNP-adsorbed 4-ATP molecule exhibits a new absorption peak with λ_{max} around 670 nm. We believe that the charge-transfer resonance from the $MoS_{2-x}O_x$ surface to the adsorbed 4-ATP molecule coupled with exciton resonance as well as with molecular resonances, and as a result, we have observed huge chemical enhancement.[16−19] As we have discussed previously, a recent report indicates that oxygen incorporation can effectively improve the

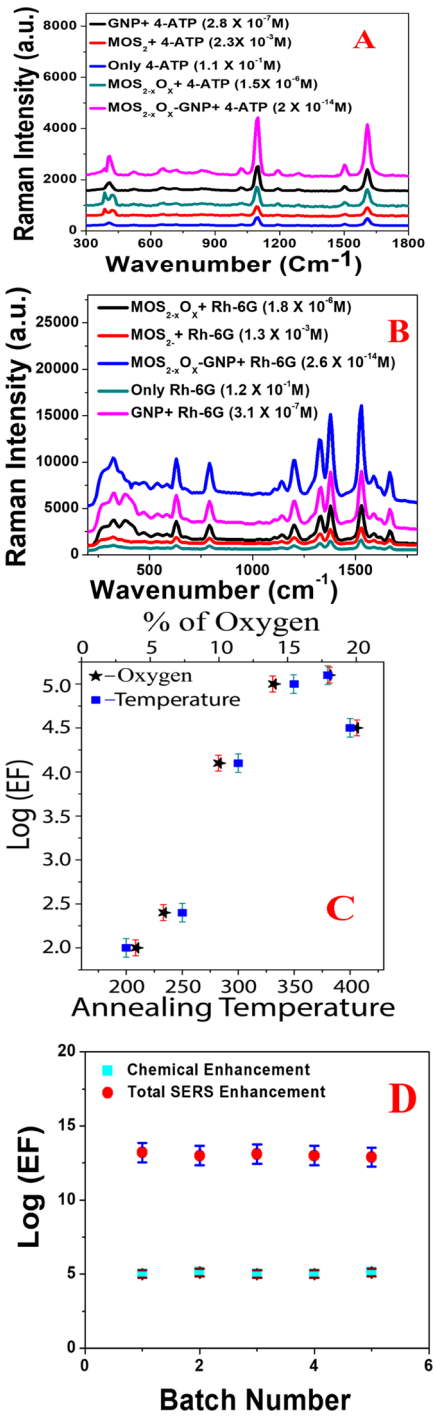

Figure 3. (A) Raman profile of 4-ATP in the presence of GNP, MoS_2, $MoS_{2-x}O_x$, GNP−$MoS_{2-x}O_x$ surface, and without any surface. (B) Raman profile of Rh-6G on MoS_2, $MoS_{2-x}O_x$, GNP, GNP−$MoS_{2-x}O_x$ surface, and without any surface. (C) Plot shows how the Raman EF for 4-ATP on $MoS_{2-x}O_x$ surface varies with annealing temperature, as well as with the percentage of oxygen incorporation. (D) Plot shows how the chemical EF and total Raman EF factor vary with samples made in different batches.

DOI: 10.1021/acsomega.9b00866
ACS Omega 2019, 4, 11112−11118

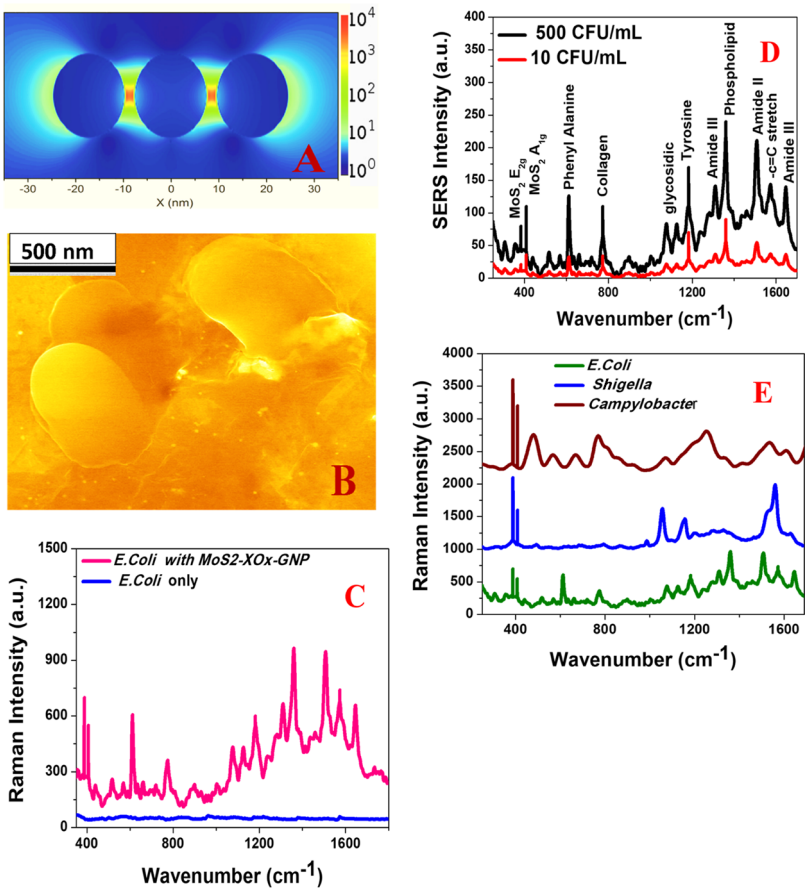

Figure 4. (A) 3D FDTD simulated electric field enhancement square ($|E|^2$) profiles for GNP assembly containing three nanoparticles. (B) SEM image shows that the drug-resistant *Campylobacter* bacteria are on the surface of 3D $MoS_{2-x}O_x$−GNP. (C) Raman spectrum shows a huge signal from drug-resistant *E. coli* (3000 cfu/mL) on 3D $MoS_{2-x}O_x$−GNP, whereas we have not observed any Raman signal from drug-resistant *E. coli* (3000 cfu/mL) in the absence of 3D $MoS_{2-x}O_x$−GNP surface. (D) Plot shows Raman spectrum from drug resistant *E. coli* at different concentrations on 3D $MoS_{2-x}O_x$−GNP. (E) Raman spectrum shows that 3D $MoS_{2-x}O_x$−GNP-based Raman can be used as a fingerprint for different bacteria such as *E. coli*, *Shigella,* and *Campylobacter*.

SERS performance of a semiconductor.[22−25] To understand better, we have also performed Raman experiment on the MoS_2 surface. Reported experimental data in Figure 3A clearly indicate that Raman EF is much higher on $MoS_{2-x}O_x$ surface than that of MoS_2 surface. From the experimental data, we found out that the Raman EF for MoS_2 surface is $\sim 2.3 \times 10^2$, whereas the EF is $\sim 1.3 \times 10^5$ for $MoS_{2-x}O_x$. To understand how oxygen incorporation affects Raman intensity, we have developed $MoS_{2-x}O_x$ surface from MoS_2 by annealing at different temperatures, where the x value should be higher at higher temperature. As reported in Figure 3C, experimental data show that the Raman EF increases as the annealing temperature increases, which is due to the high amount of oxygen incorporation. Reported data in Figure 3C also indicate that the Raman EF decreases above 400 °C, which is mainly due to the phase change as we have noted from the XRD study. We have measured the S and O ratio using EDX, XRD, and Raman data and we found out that the oxygen percentage increases from 4% at 200 °C to 20% at 350 °C. As reported in Figure 3C, experimental data show that the Raman EF increases with the high amount of oxygen incorporation. As reported in Figure 3B, from experimental data using Rh-6G as a bulk and on the surface, we have found out that the Raman EF for MoS_2 surface is $\sim 1.3 \times 10^2$ and the EF is $\sim 1.8 \times 10^5$ for $MoS_{2-x}O_x$, which is very similar to the observed data with 4-ATP. Figure 3A indicates that the Raman EF on $MoS_{2-x}O_x$ surface is comparable with the GNP surface. From experimental data using 4-ATP, we have found out that the Raman EF is $\sim 2.2 \times 10^6$ for GNP, which is around an order of magnitude higher than the $MoS_{2-x}O_x$ surface. As reported in Figure S2A in the Supporting Information, the GNP-adsorbed 4-ATP molecule exhibits a new absorption peak with λ_{max} around 670 nm, which is due to the GNP aggregation because of the interaction between GNP and 4-ATP. Very interestingly, Raman data reported in Figure 3A,B indicate that the Raman EF is $\sim 4.5 \times 10^{13}$ for GNP−$MoS_{2-x}O_x$ surface, which is around 8 orders of magnitudes higher than the $MoS_{2-x}O_x$ surface and 7 orders of magnitude higher than the GNP surface. The observed extremely high Raman EF from GNP−$MoS_{2-x}O_x$ surface is due to the strong electromagnetic as well as strong chemical enhancement capability, which provide excellent enhancement.

For our GNP−$MoS_{2-x}O_x$ surface, the GNP enhances the Raman signal via EM, and on the other hand, $MoS_{2-x}O_x$ enhances the Raman signal via a chemical enhancement mechanism. As we have reported in this manuscript, the Raman EF for only GNP is 2.2×10^6 and the same for $MoS_{2-x}O_x$ is $\sim 1.2 \times 10^5$, whereas the Raman EF is $\sim 4.5 \times 10^{13}$ for the GNP−$MoS_{2-x}O_x$ surface. We observed 2 orders of magnitude higher Raman EF for GNP. The $MoS_{2-x}O_x$ surface

DOI: 10.1021/acsomega.9b00866
ACS Omega 2019, 4, 11112−11118

is mainly due to the formation of a "hot spot" by a GNP in 3D interior and exterior surfaces, as shown in the SEM and TEM images reported in Figures 2A and S1C. To find out the origin of a synergistic enhancement mechanism, we have performed the 3D FDTD simulation to understand the "hot spot"-based plasmon coupling, which allows a huge EM enhancement mechanism.[6,11−13,35,36] Calculation details are reported in the Experimental Section and also reported previously by our group.[6,11−16] As reported in Figure 4A, FDTD simulation data show that the field enhancement for GNP aggregates in "hot spots" can be more than an order of magnitude higher than that of the individual GNP.

Because Raman EF varies with the square of field EF, we expect to increase the Raman enhancement around 2−3 orders of magnitude because of the "hot spot" formation. It is well documented that the reproducibility and stability of Raman EF are very important criteria for applications.[1−5] For this purpose, we have developed a GNP−$MoS_{2-x}O_x$ surface and only $MoS_{2-x}O_x$ surface in different batches and then monitored the reproducibility of the Raman EF using 4-ATP. Figure 3D reports the reproducibility data for Raman EF and chemical enhancement, which indicate very good reproducibility with a relative standard deviation around 6.2%.

Next, to understand whether our 3D GNP−$MoS_{2-x}O_x$ can be used for trace-level fingerprint sensing of multi-drug-resistant superbugs, we have used carbapenem-resistant *E. coli*, drug-resistant *Shigella,* and *Campylobacter*. For this purpose, we have added different superbugs such as carbapenem-resistant *E. coli*, drug-resistant *Shigella,* and *Campylobacter* at different concentrations (cfu/mL) to the GNP−$MoS_{2-x}O_x$ surface. As shown in Figure 4B, drug-resistant *Campylobacter* bacteria are on the surface of 3D $MoS_{2-x}O_x$−GNP. Figure 4C,D shows strong Raman peak from carbapenem-resistant *E. coli* even at 5 cfu/mL level. On the other hand, we have not observed the Raman peak from carbapenem-resistant *E. coli* in the absence of GNP−$MoS_{2-x}O_x$ surface, even at 3000 cfu/mL level. Although we have observed huge Raman enhancement using GNP−$MoS_{2-x}O_x$ surface, as we have not observed any Raman peak from carbapenem-resistant *E. coli* in the absence of GNP−$MoS_{2-x}O_x$ surface, as reported in Figure 4C, we are not able to determine the Raman EF using carbapenem-resistant *E. coli*. As reported in Figure 4D, in Raman spectra, we have observed in-plane (E_{2g}) Raman and out-of-plane (A_{1g}) Raman bands because of the $MoS_{2-x}O_x$ surface. On the other hand, as reported in Table 1 and Figure 4D, we have observed amide I, II, and III bands, phenyl alanine, tyrosine, collagen, phospholipid, and glycosidic bands[5−7,11,14−16,33,34] because of carbapenem-resistant *E. coli*. Raman spectra from carbapenem-resistant *E. coli*, drug-resistant *Shigella,* and *Campylobacter*, reported in Figure 4E and Table 1, clearly indicate that 3D GNP−$MoS_{2-x}O_x$ can be used for fingerprint Raman detection of different superbugs. As reported in Figure 4E, phospholipid and amide-III bands are unique for carbapenem-resistant *E. coli*, which have not been observed for drug-resistant *Shigella* and *Campylobacter*. On the other hand, guanine, tyrosine, and adenine nucleic acid bands are more prominent for *Campylobacter*, which we have not been observed for carbapenem-resistant *E. coli* and drug-resistant *Shigella*. Similarly, lipid bands near 1480 cm^{-1} are unique for *Shigella*.

3. CONCLUSIONS

In conclusion, our findings reveal that the 3D $MoS_{2-x}O_x$−GNP hybrid provides immense Raman enhancement via giant chemical enhancement mechanisms, as well synergistic plasmonic enhancement mechanism. Reported data show that because of the presence of $MoS_{2-x}O_x$ in our hybrid, the chemical EF is ~10^5, which is comparable with plasmonic EF by plasmonic nanoparticle. We have demonstrated that oxygen incorporation on MoS_2 can effectively improve the SERS performance via a strong chemical enhancement mechanism, which is due to the photon-induced charge transfer from the $MoS_{2-x}O_x$ surface to the adsorbed molecule. On the other hand, the total Raman EF is ~10^{13} from GNP−$MoS_{2-x}O_x$ hybrid because of the synergistic effect of electromagnetic and chemical enhancement mechanisms. The reported synergistic Raman EF is mainly due to the "hot spot" formation by GNP in 3D interior and exterior surfaces. Our experimental results show that the GNP−$MoS_{2-x}O_x$ hybrid has the capability for ultrasensitive label-free sensing of carbapenem-resistant *E. coli*, drug-resistant *Shigella,* and *Campylobacter*, even at 5 cfu/mL concentration level.

Table 1. Fingerprint Raman Modes Observed from Drug-Resistant *E. coli*, *Shigella*, and *Campylobacter*[a]

Raman peak (cm^{-1}) for *E. coli*	Raman peak (cm^{-1}) for *Shigella*	Raman peak (cm^{-1}) for *Campylobacter*	vibration mode
1646			amide I
1574			adenine guanine ring stretching
	1480		lipid
1507			amide II
1301			amide III
		1240	DNA/RNA bases
	1180		phospholipids
	1110		fatty acid in lipids
		814	−O−P−O− for DNA
780			Collagen
		747	tyrosine
		676	guanine

[a]All the bands have been assigned using reported data from different microorganisms.[5−7,11,14−16,33,34]

4. EXPERIMENTAL SECTION

Molybdenum(VI) oxide powder, sodium sulfide (Na_2S) and HCl, different solvents, and other chemicals were purchased from Sigma-Aldrich (St. Louis, MO, USA). Superbugs such as carbapenem-resistant *E. coli*, drug-resistant *Shigella,* and *Campylobacter* and growth media were purchased from American Type Culture Collection (ATCC, Rockville, MD).

4.1. Synthesis of the Gold Nanoparticles. Spherical-shaped gold nanoparticles (AuNPs) were synthesized according to the previous work by our group.[6,11−16] For this purpose, we have used 1.25 mL of 10 mM $HAuCl_4$ solution and 2 mL of 1% trisodium citrate dihydrate. At the end, the purified AuNPs were characterized by a microscopic technique, as reported in Figure S1A.

4.2. Synthetic Procedure of MoS_2 Nanosheets. A facile hydrothermal synthetic method was adopted for the synthesis of $MoS_{2-x}O_x$ nanosheets. In a typical experiment, 0.72 g of molybdenum(VI) oxide (MoO_3) powder and 3.6 g of sodium sulfide (Na_2S) were mixed gently and the mixture was transferred into a Teflon-lined stainless steel autoclave of capacity 100 mL. Then, approximately 70 mL of 0.2 N HCl

DOI: 10.1021/acsomega.9b00866
ACS Omega 2019, 4, 11112−11118

was added to fill the autoclave up to 75−80% of the total volume. After that, the autoclave was tightly sealed, maintained at 200 °C overnight, and then cooled to room temperature. A black precipitate was obtained by centrifugation from the final reaction products and washed successively with distilled water and ethanol several times. Finally, the semisolid $MoS_{2-x}O_x$ nanosheets were dried in vacuum at 60 °C for 6 h. The pure products are characterized by SEM and other spectroscopic and microscopic techniques, as reported in Figure S1.

4.3. Synthesis of the MoS_2−GNP Hybrid. To synthesize AuNP-decorated MoS_2 nanosheets, 5.0 mL of 10 nM gold nanoparticle solution was dropped in 10 mL of 5 ppm of dispersed in freshly prepared MoS_2 solutions in phosphate-buffered saline (PBS) buffer and the mixture was sonicated for 2 h at room temperature. The mixture was continuously stirred at very low speed overnight at room temperature for the completion of the reaction. To remove excess regents and buffer solution, the mixed solution was washed with methanol two to three times by centrifugation at 5000 rpm for 15 min followed by decantation. Finally, the AuNP-decorated MoS_2 pellet was dried under vacuum at room temperature for a week. Figure S1D shows the TEM image of freshly prepared MoS_2−GNP hybrid.

4.4. Synthetic Procedure of $MoS_{2-x}O_x$ Nanosheets. Because it is now well-known that oxygen incorporation is the effective way to improve the SERS performance of nonmetal oxide semiconductors,[12−19] in the next step, we have synthesized a 2D $MoS_{2-x}O_x$ nanosheet. For this purpose, we have developed a $MoS_{2-x}O_x$ nanosheet, via annealing of 2D MoS_2 at 350 °C temperature in air. The pure products are characterized by SEM and other spectroscopic and microscopic techniques, as reported in Figure S1.

4.5. Synthesis of the $MoS_{2-x}O_x$−GNP Hybrid. To synthesize AuNP-decorated $MoS_{2-x}O_x$ nanosheets, 5.0 mL of 10 nM gold nanoparticle solution was dropped in 10 mL of 5 ppm of dispersed in freshly prepared $MoS_{2-x}O_x$ solutions in PBS buffer and the mixture was sonicated for 2 h at room temperature. The mixture was continuously stirred at very low speed overnight at room temperature for the completion of the reaction. To remove excess regents and buffer solution, the mixed solution was washed with methanol two to three times by centrifugation at 5000 rpm for 15 min followed by decantation. Finally, the AuNP-decorated $MoS_{2-x}O_x$ pellet was dried under vacuum at room temperature for a week. After that, the purified $MoS_{2-x}O_x$−GNP hybrid was characterized by powder XRD, high-resolution tunneling electron microscopy, EDX spectroscopy, and Raman spectroscopy, as reported in Figure S1A−G. The elemental molar ratios for $MoS_{2-x}O_x$−GNP hybrid were determined using inductively coupled plasma−mass spectrometer data and EDX data.

4.6. Superbug Sample Preparation. Carbapenem-resistant *E. coli*, drug-resistant *Shigella,* and *Campylobacter* superbugs were cultured according to the ATCC protocol, as we have reported previously.[6,11−16]

4.7. Raman Experimental Details. We have used a portable Raman probe for the fingerprint detection of different superbugs, as we have reported previously.[6,11−16] For the Raman experiments using $MoS_{2-x}O_x$−GNP hybrid and other materials, we have used 670 nm light as the excitation light source and a QE65000 spectrometer for Raman data collection.

4.8. 3D FDTD Simulation. We have used the 3D FDTD simulation age for full-field electromagnetic wave calculations, as we have reported previously.[6,11−16] For the calculation, we have used a gold nanoparticle of 30 nm diameter which is decorated on the $MoS_{2-x}O_x$ nanosheet as we have observed experimentally. 670 nm was used as the incident wavelength and the entire process has been performed under 0.001 nm mesh resolution and 4000 fs duration.[11−16]

■ ASSOCIATED CONTENT

Supporting Information

The Supporting Information is available free of charge on the ACS Publications website at DOI: 10.1021/acsomega.9b00866.

Microscopic and spectroscopic characterization data (PDF)

■ AUTHOR INFORMATION

Corresponding Author

*E-mail: paresh.c.ray@jsums.edu. Fax: +16019793674.

ORCID

Avijit Pramanik: 0000-0002-4623-2099

Paresh Chandra Ray: 0000-0001-5398-9930

Notes

The authors declare no competing financial interest.

■ ACKNOWLEDGMENTS

Dr. Ray thanks NSF-PREM grant no. DMR-1205194 and NSF CREST grant no. 1547754 for their generous funding.

■ REFERENCES

(1) Lane, L. A.; Qian, X.; Nie, S. SERS Nanoparticles in Medicine: From Label-Free Detection to Spectroscopic Tagging. *Chem. Rev.* **2015**, *115*, 10489−10529.

(2) Ding, S.-Y.; You, E.-M.; Tian, Z.-Q.; Moskovits, M. Electromagnetic theories of surface-enhanced Raman spectroscopy. *Chem. Soc. Rev.* **2017**, *46*, 4042−4076.

(3) Cong, S.; Wang, Z.; Gong, W.; Chen, Z.; Lu, W.; Lombardi, J.; Zhao, J. Electrochromic semiconductors as colorimetric SERS substrates with high reproducibility and renewability. *Nat. Commun.* **2019**, *10*, 678.

(4) Henry, A.-I.; Sharma, B.; Cardinal, M. F.; Kurouski, D.; Van Duyne, R. P. Surface-Enhanced Raman Spectroscopy Biosensing: In Vivo Diagnostics and Multimodal Imaging. *Anal. Chem.* **2016**, *88*, 6638−6647.

(5) Li, J.-F.; Zhang, Y.-J.; Ding, S.-Y.; Panneerselvam, R.; Tian, Z.-Q. Core-Shell Nanoparticle-Enhanced Raman Spectroscopy. *Chem. Rev.* **2017**, *117*, 5002−5069.

(6) Sinha, S. S.; Jones, S.; Pramanik, A.; Ray, P. C. Nanoarchitecture Based SERS for Biomolecular Fingerprinting and Label-Free Disease Markers Diagnosis. *Acc. Chem. Res.* **2016**, *49*, 2725−2735.

(7) Cialla-May, D.; Zheng, X.-S.; Weber, K.; Popp, J. Recent Progress in Surface-Enhanced Raman Spectroscopy for Biological and Biomedical Applications: From Cells to Clinics. *Chem. Soc. Rev.* **2017**, *46*, 3945−3961.

(8) Cardinal, M. F.; Vander Ende, E.; Hackler, R. A.; McAnally, M. O.; Stair, P. C.; Schatz, G. C.; Van Duyne, R. P. Expanding Applications of SERS through Versatile Nanomaterials Engineering. *Chem. Soc. Rev.* **2017**, *46*, 3886−3903.

(9) Matricardi, C.; Hanske, C.; Garcia-Pomar, J. L.; Langer, J.; Mihi, A.; Liz-Marzán, L. M. Gold Nanoparticle Plasmonic Superlattices as Surface-Enhanced Raman Spectroscopy Substrates. *ACS Nano* **2018**, *12*, 8531−8539.

(10) DeJesus, J. F.; Trujillo, M. J.; Camden, J. P.; Jenkins, D. M. N-Heterocyclic Carbenes as a Robust Platform for Surface-Enhanced Raman Spectroscopy. *J. Am. Chem. Soc.* **2018**, *140*, 1247−1250.

DOI: 10.1021/acsomega.9b00866
ACS Omega 2019, 4, 11112−11118

(11) Jones, S.; Sinha, S. S.; Pramanik, A.; Ray, P. C. Three-dimensional (3D) plasmonic hot spots for label-free sensing and effective photothermal killing of multiple drug resistant superbugs. *Nanoscale* **2016**, *8*, 18301−18308.
(12) Fan, Z.; Kanchanapally, R.; Ray, P. C. Hybrid Graphene Oxide Based Ultrasensitive SERS Probe for Label-Free Biosensing. *J. Phys. Chem. Lett.* **2013**, *4*, 3813−3818.
(13) Singh, A. K.; Khan, S. A.; Fan, Z.; Demeritte, T.; Senapati, D.; Kanchanapally, R.; Ray, P. C. Development of a Long-Range Surface-Enhanced Raman Spectroscopy Ruler. *J. Am. Chem. Soc.* **2012**, *134*, 8662−8669.
(14) Paul, A. M.; Fan, Z.; Sinha, S. S.; Shi, Y.; Le, L.; Bai, F.; Ray, P. C. Bioconjugated Gold Nanoparticle Based SERS Probe for Ultrasensitive Identification of Mosquito-Borne Viruses Using Raman Fingerprinting. *J. Phys. Chem. C* **2015**, *119*, 23669−23675.
(15) Demeritte, T.; Viraka Nellore, B. P.; Kanchanapally, R.; Sinha, S. S.; Pramanik, A.; Chavva, S. R.; Ray, P. C. Hybrid Graphene Oxide Based Plasmonic-Magnetic Multifunctional Nanoplatform for Selective Separation and Label-Free Identification of Alzheimer's Disease Biomarkers. *ACS Appl. Mater. Interfaces* **2015**, *7*, 13693−13700.
(16) Fan, Z.; Yust, B.; Nellore, B. P. V.; Sinha, S. S.; Kanchanapally, R.; Crouch, R. A.; Pramanik, A.; Chavva, S. R.; Sardar, D.; Ray, P. C. Accurate Identification and Selective Removal of Rotavirus Using a Plasmonic-Magnetic 3D Graphene Oxide Architecture. *J. Phys. Chem. Lett.* **2014**, *5*, 3216−3221.
(17) Bodelón, G.; Montes-García, V.; López-Puente, V.; Hill, E. H.; Hamon, C.; Sanz-Ortiz, M. N.; Rodal-Cedeira, S.; Costas, C.; Celiksoy, S.; Pérez-Juste, I.; Scarabelli, L.; La Porta, A. Detection and Imaging of Quorum Sensing in Pseudomonas aeruginosa Biofilm Communities by Surface-Enhanced Resonance Raman Scattering. *Nat. Mater.* **2016**, *15*, 1203−1211.
(18) Shutov, A. D.; Yi, Z.; Wang, J.; Sinyukov, A. M.; He, Z.; Tang, C.; Chen, J.; Ocola, E. J.; Laane, J.; Sokolov, A. V.; Voronine, D. V.; Scully, M. O. Giant Chemical Surface Enhancement of Coherent Raman Scattering on MoS2. *ACS Photonics* **2018**, *5*, 4960−4968.
(19) Tan, Y.; Ma, L.; Gao, Z.; Chen, M.; Chen, F. Two-Dimensional Heterostructure as a Platform for Surface-Enhanced Raman Scattering. *Nano Lett.* **2017**, *17*, 2621−2626.
(20) Zheng, Z.; Cong, S.; Gong, W.; Xuan, J.; Li, G.; Lu, W.; Geng, F.; Zhao, Z. Semiconductor SERS Enhancement Enabled by Oxygen Incorporation. *Nat. Commun.* **2017**, *8*, 1993.
(21) Liu, W.; Bai, H.; Li, X.; Li, W.; Zhai, J.; Li, J.; Xi, G. Improved surface-enhanced Raman spectroscopy sensitivity on metallic tungsten oxide by the synergistic effect of surface plasmon resonance coupling and charge transfer. *J. Phys. Chem. Lett.* **2018**, *9*, 4096−4100.
(22) Zhang, Q.; Li, X.; Ma, Q.; Zhnag, Q.; Bai, H.; Yi, W.; Liu, J.; Han, J.; Xi, G. A metallic molybdenum dioxide with high stability for surface enhanced Raman spectroscopy. *Nat. Commun.* **2017**, *8*, 14903.
(23) Su, S.; Zhang, C.; Yuwen, L.; Chao, J.; Zuo, X.; Liu, X.; Song, C.; Fan, C.; Wang, L. Creating SERS Hot Spots on MoS2 Nanosheets with in Situ Grown Gold Nanoparticles. *ACS Appl. Mater. Interfaces* **2014**, *6*, 18735−18741.
(24) Muehlethaler, C.; Considine, C. R.; Menon, V.; Lin, W.-C.; Lee, Y.-H.; Lombardi, J. R. Ultrahigh Raman Enhancement on Monolayer MoS2. *ACS Photonics* **2016**, *3*, 1164−1169.
(25) Lin, J.; Liang, L.; Ling, X.; Zhang, S.; Mao, N.; Zhang, N.; Sumpter, B. G.; Meunier, V.; Tong, L.; Zhang, J. Enhanced Raman Scattering on in-Plane Anisotropic Layered Materials. *J. Am. Chem. Soc.* **2015**, *137*, 15511−15517.
(26) Ling, X.; Fang, W.; Lee, Y.-H.; Araujo, P. T.; Zhang, X.; Rodriguez-Nieva, J. F.; Lin, Y.; Zhang, J.; Kong, J.; Dresselhaus, M. S. Raman Enhancement Effect on Two-Dimensional Layered Materials: Graphene, h-BN and MoS2. *Nano Lett.* **2014**, *14*, 3033−3040.
(27) Tan, Y.; Ma, L.; Gao, Z.; Chen, M.; Chen, F. Two-Dimensional Heterostructure as a Platform for Surface-Enhanced Raman Scattering. *Nano Lett.* **2017**, *17*, 2621−2626.
(28) Huang, S.; Ling, X.; Liang, L.; Song, Y.; Fang, W.; Zhang, J.; Kong, J.; Meunier, V.; Dresselhaus, M. S. Molecular Selectivity of Graphene-Enhanced Raman Scattering. *Nano Lett.* **2015**, *15*, 2892−2901.
(29) Yan, D.; Qiu, W.; Chen, X.; Liu, L.; Lai, Y.; Meng, Z.; Song, J.; Liu, Y.; Liu, X.-Y.; Zhan, D. Achieving High-Performance Surface-Enhanced Raman Scattering through One-Step Thermal Treatment of Bulk MoS2. *J. Phys. Chem. C* **2018**, *122*, 14467−14473.
(30) Cong, S.; Yuan, Y.; Chen, Z.; Hou, J.; Yang, M.; Su, Y.; Zhang, Y.; Li, L.; Li, Q.; Geng, F.; Zhao, Z. Noble Metal-Comparable SERS Enhancement from Semiconducting Metal Oxides by Making Oxygen Vacancies. *Nat. Commun.* **2015**, *6*, 7800.
(31) Lee, Y.; Kim, H.; Lee, J.; Yu, S. H.; Hwang, E.; Lee, C.; Ahn, J.-H.; Cho, J. H. Enhanced Raman Scattering of Rhodamine 6G Films on Two-Dimensional Transition Metal Dichalcogenides Correlated to Photoinduced Charge Transfer. *Chem. Mater.* **2016**, *28*, 180−187.
(32) Cai, Q.; Mateti, S.; Yang, W.; Jones, R.; Watanabe, K.; Taniguchi, T.; Huang, S.; Chen, Y.; Li, L. H. Boron Nitride Nanosheets Improve Sensitivity and Reusability of Surface-Enhanced Raman Spectroscopy. *Angew. Chem., Int. Ed.* **2016**, *55*, 8405−8409.
(33) Stöckel, S.; Kirchhoff, J.; Neugebauer, U.; Rösch, P.; Popp, J. The application of Raman spectroscopy for the detection and identification of microorganisms. *J. Raman Spectrosc.* **2016**, *47*, 89−109.
(34) Lorenz, B.; Wichmann, C.; Stöckel, S.; Rösch, P.; Popp, J. Cultivation-Free Raman Spectroscopic Investigations of Bacteria. *Trends Microbiol.* **2017**, *25*, 413−424.
(35) Zhao, J.; Pinchuk, A. O.; McMahon, J. M.; Li, S.; Ausman, L. K.; Atkinson, A. L.; Schatz, G. C. Methods for Describing the Electromagnetic Properties of Silver and Gold Nanoparticles. *Acc. Chem. Res.* **2008**, *41*, 1710−1720.
(36) Knight, M. W.; King, N. S.; Liu, L.; Everitt, H. O.; Nordlander, P.; Halas, N. J. Aluminum for Plasmonics. *ACS Nano* **2014**, *8*, 834−840.

DOI: 10.1021/acsomega.9b00866
ACS Omega 2019, 4, 11112−11118